JGR Space Physics

RESEARCH ARTICLE
10.1029/2025JA034737

Global Morphology of Chorus Waves in the Outer Radiation Belt and the Effect of Geomagnetic Activity and f_{pe}/f_{ce}

K. A. Bunting[1], N. P. Meredith[1], J. Bortnik[2], Q. Ma[2,3], R. Matsuura[2], and X.-C. Shen[3]

[1]British Antarctic Survey, Cambridge, UK, [2]Department of Atmospheric and Oceanic Sciences, UCLA, Los Angeles, CA, USA, [3]Center for Space Physics, Boston University, Boston, MA, USA

Key Points:

- Equatorial chorus in the frequency range f_{lhr}–0.1 f_{ce} is strongest for $f_{pe}/f_{ce} > 10$ when AE > 200 nT for $L^* = 5$–8, from 22 to 12 MLT
- Equatorial chorus in the frequency range 0.3–0.4 f_{ce} is independent of f_{pe}/f_{ce} and strongest when AE > 200 nT for $L^* = 3.5$–8, from 21 to 12 MLT
- Equatorial chorus in the frequency range 0.5–0.7 f_{ce} is strongest for $f_{pe}/f_{ce} < 6$ when AE > 200 nT for $L^* = 4$–6, from 21 to 09 MLT

Correspondence to:
K. A. Bunting,
kantin@bas.ac.uk

Citation:
Bunting, K. A., Meredith, N. P., Bortnik, J., Ma, Q., Matsuura, R., & Shen, X.-C. (2026). Global morphology of chorus waves in the outer radiation belt and the effect of geomagnetic activity and f_{pe}/f_{ce}. *Journal of Geophysical Research: Space Physics*, *131*, e2025JA034737. https://doi.org/10.1029/2025JA034737

Received 7 OCT 2025
Accepted 2 JAN 2026

Author Contributions:
Conceptualization: K. A. Bunting, N. P. Meredith
Data curation: K. A. Bunting, X.-C. Shen
Formal analysis: K. A. Bunting, N. P. Meredith
Funding acquisition: N. P. Meredith
Investigation: K. A. Bunting, N. P. Meredith, J. Bortnik, Q. Ma, R. Matsuura
Methodology: K. A. Bunting, N. P. Meredith, J. Bortnik, Q. Ma, R. Matsuura
Project administration: N. P. Meredith
Resources: K. A. Bunting, N. P. Meredith
Software: K. A. Bunting
Supervision: N. P. Meredith
Validation: K. A. Bunting, N. P. Meredith
Visualization: K. A. Bunting
Writing – original draft: K. A. Bunting, N. P. Meredith

Abstract Whistler-mode chorus waves play a key role in driving radiation belt dynamics by enabling both acceleration of electrons to relativistic energies as well as their loss into the atmosphere via pitch-angle scattering. The ratio between the electron plasma frequency (f_{pe}) and the electron gyrofrequency (f_{ce}) significantly influences the efficiency of these processes, with electron acceleration being most effective during periods of low f_{pe}/f_{ce}. In this study, a combined total of approximately 24.5 years of Time History of Events and Macroscale Interactions during Substorms (THEMIS) wave data are analyzed to show how chorus wave intensity and spatial location vary with relative frequency, geomagnetic activity and f_{pe}/f_{ce}. Results demonstrate that the strongest chorus emissions are observed during active conditions (AE > 200 nT). At these times, equatorial chorus at low relative frequencies ($f_{lhr} < f < 0.1\,f_{ce}$) is strongest when f_{pe}/f_{ce} is high ($f_{pe}/f_{ce} > 10$) primarily in the region $5 < L^* < 8$, from 22:00–12:00 MLT. In sharp contrast at high relative frequencies ($0.5\,f_{ce} < f < 0.7\,f_{ce}$), the equatorial chorus is strongest when f_{pe}/f_{ce} is low ($f_{pe}/f_{ce} < 6$) mainly in the region $4 < L^* < 6$ from 21:00–09:00 MLT. At intermediate relative frequencies ($0.3\,f_{ce} < f < 0.4\,f_{ce}$), equatorial chorus is strongest in the region $3.5 < L^* < 8$ and are largely independent of f_{pe}/f_{ce} from 21:00–12:00 MLT. In the off-equatorial region the strongest waves are seen in the frequency range ($0.1\,f_{ce} < f < 0.3\,f_{ce}$) between $5 < L^* < 8$ and 06:00–15:00 MLT and again are mostly independent of f_{pe}/f_{ce}. We show that the location of the strongest waves can be largely explained in terms of the source electrons being in the required energy range for resonance and the absence of Landau damping and highlight the regions where electron acceleration to relativistic energies is likely to be mostly significant.

Plain Language Summary Chorus waves are naturally occurring plasma waves often observed in the terrestrial radiation belts that strongly influence the behavior of energetic electrons. These waves can both accelerate electrons to relativistic energies as well as scatter electrons into Earth's atmosphere, where they are consequently lost. A key factor which influences the efficiency of these processes is the ratio of two frequencies (the plasma frequency and the electron gyrofrequency). We analyze a combined 24.5 years of wave measurements from the THEMIS spacecraft to show how chorus wave intensity and spatial location vary with relative frequency, geomagnetic activity and this frequency ratio (f_{pe}/f_{ce}). The strongest waves are generally observed on the dawn side of the Earth during active geomagnetic conditions. At intermediate relative frequencies, strong waves can occur across a wide range of f_{pe}/f_{ce} values. In contrast, at low and high frequencies, strong waves are most often associated with high and low f_{pe}/f_{ce} values respectively. We show that the location of the strongest waves can be largely explained in terms of the source electrons being in the required energy range for resonance and the absence of Landau damping and highlight regions where electron acceleration to relativistic energies is likely to be most significant.

1. Introduction

Chorus waves represent a class of whistler-mode electromagnetic waves, which are right-hand polarized and characterized by 0.1 s repetitive bursts occurring in the frequency range above the lower hybrid resonance frequency (f_{lhr}) and below the electron gyrofrequency (f_{ce}) (Li et al., 2012; Santolík et al., 2004; Tsurutani & Smith, 1977). These emissions are known as chorus since the observed rising tones, or less frequent falling tones, often resemble a "chorus" of singing birds at dawn when converted to audio. Chorus waves are generated in the near-equatorial region outside of the plasmapause (Burtis & Helliwell, 1969; Inan et al., 2004; Koons & Roeder, 1990; Lauben et al., 2002) by anisotropic distributions of energetic electrons with energies in the range of approximately keV to 100 keV (Li, Thorne, Bortnik, et al., 2010; Omura et al., 2008), which are injected into the inner magnetosphere during both geomagnetic storms and substorms. Consequently, chorus is observed largely

Writing – review & editing:
K. A. Bunting, N. P. Meredith, J. Bortnik, Q. Ma, R. Matsuura

outside the plasmapause and is substorm dependent, with the largest intensities being seen during active conditions (O. V. Agapitov et al., 2018; Li et al., 2009; Meredith et al., 2001, 2012, 2020; Miyoshi et al., 2013; Santolík et al., 2003; Tsurutani & Smith, 1977). Chorus waves are generally observed in two distinct bands, between 0.1 and 0.5 f_{ce} (lower-band chorus) and 0.5–0.8 f_{ce} (upper-band chorus) (Burtis & Helliwell, 1969; Koons & Roeder, 1990), with a power gap at 0.5 f_{ce} (Tsurutani & Smith, 1977).

Chorus has been shown to play a significant role in the formation of the diffuse aurora (Thorne, 2010), while storm-time chorus at high latitudes can drive microburst precipitation (Lorentzen et al., 2001), leading to formation of the pulsating aurora (Namekawa et al., 2023; Nishimura et al., 2010; Thorne et al., 2005). It has also been shown that by propagating into the plasmasphere, chorus is a significant source of the unstructured plasmaspheric hiss (Bortnik et al., 2008, 2009; Meredith et al., 2013), another important magnetospheric emission, which is largely responsible for the formation of the slot region between the inner and outer radiation belts (Abel & Thorne, 1998a, 1998b; Albert, 1994; Lyons et al., 1972; Lyons & Thorne, 1973; Meredith et al., 2007, 2009) and contributes to electron loss in the outer radiation belt during and following geomagnetic storms (Lam et al., 2007; Ma et al., 2016, 2022; Meredith et al., 2006; Summers et al., 2007a; Thorne et al., 1973). Furthermore, plasmaspheric hiss has also been shown to "leak" out of the plasmapause (Feng et al., 2023; Zhu et al., 2015). This unstructured emission outside of the plasmasphere is known as exohiss (Thorne et al., 1973; Zhu et al., 2015).

Wave-particle interactions of energetic electrons with chorus have been shown to play a key role in the dynamics of the radiation belts, specifically the loss of keV-MeV electrons into the terrestrial atmosphere via pitch angle scattering (Summers et al., 2007a, 2007b; Thorne et al., 2005) and the acceleration of electrons with energies of hundreds of keV, up to MeV range in the Earth's outer radiation belt (Allison et al., 2021; Horne et al., 2005; Horne & Thorne, 1998; Jaynes et al., 2015; Meredith et al., 2002; Thorne et al., 2013). These "killer" MeV electrons (Graham, 1994) can damage satellites traveling in this region by deep dielectric charging leading to operational challenges and affecting the longevity of onboard electronics (J.-Z. Wang et al., 2018; Wrenn et al., 2002).

Traditionally, wave-particle interactions are included as a diffusive process in Earth's radiation belt models (Glauert et al., 2014). In order to calculate the diffusion rates, quasi-linear theory is applied and specifically the variations in intensity with frequency, L^*, magnetic local time (MLT), magnetic latitude (λ_m) and geomagnetic activity are input (e.g., O. Agapitov et al., 2019; Glauert & Horne, 2005; Horne et al., 2013; Wong et al., 2024). The ratio of plasma frequency (f_{pe}) to the electron gyrofrequency (f_{ce}) is also a very important factor in determining the efficiency of the wave-particle interactions (Horne et al., 2003). Acceleration due to chorus is most efficient for lower-band chorus (Horne & Thorne, 1998) in regions of low f_{pe}/f_{ce}, where the increased wave phase velocity enhances energy exchange and enables seed electrons at large pitch angles to be accelerated to MeV energies (Horne & Thorne, 2003; Meredith et al., 2002; Summers et al., 1998), while simultaneously scattering low energy source electrons into the loss cone. However at high values of f_{pe}/f_{ce} ($f_{pe}/f_{ce} > 7$), chorus waves primarily drive pitch-angle scattering with minimal energy exchange and loss of electrons to the atmosphere (Lyons et al., 1972; Meredith et al., 2006; Summers et al., 1998, 2005).

Previous statistical studies using data from the CRRES mission (Meredith et al., 2003) and the Van Allen Probes (O. Agapitov et al., 2019) have investigated the effects of f_{pe}/f_{ce} and geomagnetic activity on lower-band chorus, highlighting regions favorable for strong electron acceleration. These studies demonstrated regions in which electron acceleration to relativistic energies is most favorable. Meredith et al. (2003) suggested acceleration is strongest between $4 < L < 6$ between 3:00–10:00 MLT in the equatorial region and 6:00–14:00 MLT in the mid-latitude region. More recently O. Agapitov et al. (2019) suggested chorus acceleration is likely to be strongest from $\sim 2.7 < L < 4$ between 21:00–09:00 MLT, and from $3.5 < L < 5.5$ between 21:00–04:00 MLT. However, the orbits of both the CRRES and Van Allen Proves are restricted to $L^* \approx 6$ in the equatorial region and therefore do not extend beyond geosynchronous orbit.

In this study, a new chorus wave database is developed, binned as a function of relative frequency, location (L^*, MLT, λ_m), geomagnetic activity and additionally the local f_{pe}/f_{ce} ratio. A combined total of approximately 24.5 years of wave data is analyzed from three Time History of Events and Macroscale Interactions during Substorms (THEMIS) satellites; namely THEMIS-A, -D and -E. Thus, allowing favorable regions of electron acceleration and loss to be identified from inside geosynchronous orbit out to $L^* \approx 10$. This new and extensive database provides good coverage and statistics, allowing us to clearly observe differences in varying geomagnetic

conditions. The associated instrumentation and data analysis is outlined in Section 2. Average chorus intensities as a function of relative frequency, geomagnetic activity, location (L^*, MLT) and f_{pe}/f_{ce} are presented in the equatorial and off-equatorial regions in Sections 3.1 and 3.2 respectively. Finally, our results are discussed and conclusions presented in Sections 4 and 5 respectively.

2. Instrumentation Data Analysis

2.1. Instrumentation

The five NASA THEMIS spacecraft were launched on 17 February 2007 into near equatorial orbits ($|\lambda_m| < 25°$), with apogees exceeding 10 R_E and perigees below 2 R_E (Angelopoulos, 2008). In this study, data is analyzed from the three THEMIS spacecraft, namely THEMIS-A, -D and -E, that sample whistler-mode waves in the inner magnetosphere.

The wave data used in this study were collected by the Search Coil Magnetometer (SCM) (Le Contel et al., 2008; Roux et al., 2008). This instrument observes the magnetic field fluctuations between 0.1 Hz and 4 kHz. High resolution (fff) data consists of two components of the wave spectral density ($B_{\parallel}$ and $B_{\perp}$), which are obtained by averaging spectra over 0.5 or 1 s at 8 s resolution in logarithmically spaced frequency bins (Cully et al., 2008) with approximately 12 hr of coverage per day. In this study, approximately 11.75 years of THEMIS -A fff magnetic wave spectral data (20/04/2010–31/12/2021), 6.5 years of THEMIS-D data (22/03/2011–12/09/2017) and 6.25 years THEMIS-E data (22/03/2011–29/05/2017) are analyzed, providing a combined total of ∼24.5 years of wave data. THEMIS-D and -E data only extends to 2017 due to a hardware issue affecting the perpendicular component of the magnetic field data. After these dates, the data shows a significant change in the spectral density background due to hardware damage, rendering chorus and other emissions indistinguishable from background noise.

The electron gyrofrequency is calculated from the ambient magnetic field data which is locally measured by the THEMIS Fluxgate Magnetometer (FGM) with a ∼4 Hz sampling rate (Auster et al., 2008). At $L^* \approx 4$, the electron gyrofrequency can become large and can substantially exceed the 4 kHz upper limit of the SCM, which limits observations of upper-band chorus in this region. The total plasma density is derived via the spacecraft potential, as measured by the Electric Field Instrument (EFI), and the electron thermal speed as measured by the Electrostatic analyzer (ESA) instrument (see Mozer (1973) and Pedersen et al. (1998)). Multiple validation analyses show that the uncertainty in the total plasma density derived via this method is typically within a factor of 2 (Kwon et al., 2015; Li, Thorne, Nishimura, et al., 2010; Min et al., 2012). The inferred plasma densities are then used to derive f_{pe} and f_{pe}/f_{ce}. As f_{pe} is proportional to the root of the density, the corresponding uncertainty in f_{pe} is ∼40%. The uncertainty within f_{pe}/f_{ce} is also dominated by this factor, as f_{ce} is measured with high precision from the FGM.

2.2. Data Analysis

The wave spectral density data show a frequency dependent noise response. Therefore, it is imperative that the background is quantified and removed from the data. Here, the method initially proposed by Malaspina et al. (2017) is used and adapted to quantify the background noise level as a function of frequency. Firstly, all wave spectral data from each satellite and magnetic component are compiled into distributions of samples versus power spectral density. The noise threshold (t_i) is then calculated by fitting a gaussian to the peak of the power distribution. The noise threshold is defined as $t_i = \mu + 2\sigma$ where μ and σ are the mean and standard deviation of the fitted gaussian. This process is repeated independently for each frequency of both fff components ($B_{\parallel}$ and $B_{\perp}$) on each satellite. The noise thresholds for $B_{\perp}$ and $B_{\parallel}$ for THEMIS -A, -D and -E are plotted as a function of frequency in Figures 1a and 1b respectively. Figure 1 shows the SCM noise thresholds follow a similar trend with the highest noise level being found at the lowest frequency bands, and reducing to a minima at approximately 1 kHz, before rising toward the highest frequencies. The corresponding background threshold is then subtracted from all data within a given frequency band. The high power anomalies are also removed. These are defined as emissions that occur above the lowest power bin exceeding $\mu + 3\sigma$ in which the number of samples fall below 5. Finally, the total magnetic wave spectral data (B_{tot}) is calculated by: $B_{tot} = \sqrt{B_{\parallel}^2 + 2B_{\perp}^2}$.

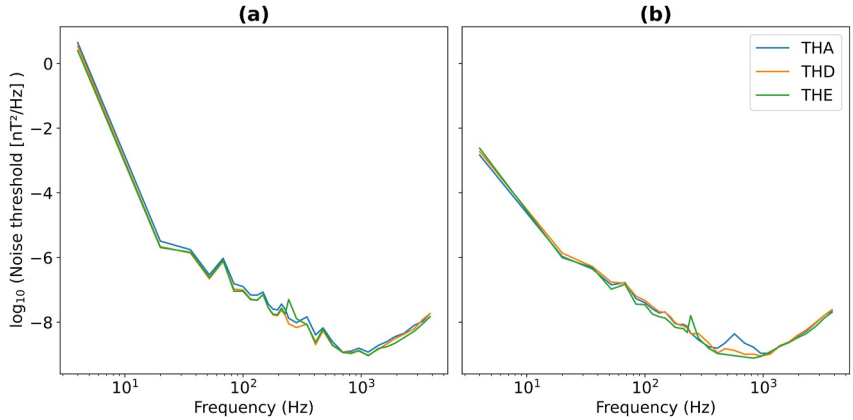

Figure 1. Plots of the noise thresholds as a function of frequency for (a) $B_{\perp}$ and (b) $B_{\parallel}$ for Time History of Events and Macroscale Interactions during Substorms -A; blue, -D; orange and -E; green.

On occasion, the fff magnetic wave spectral data show abnormally high intensities that last for 1–2 time steps. We found that these high-intensities occur due to a change in FGM mode as the satellite moves closer to Earth, where a greater FGM range is required. Care is taken to remove these features. L^* is computed using the TS04 external magnetic field model (Tsyganenko & Sitnov, 2005) and the International Geomagnetic Reference Field. An approximation of 90° pitch angle was used to calculate L^*.

Chorus waves overlap in frequency with various other electromagnetic emissions in the terrestrial radiation belts such as plasmaspheric hiss and lightning generated whistlers. However, chorus waves are exclusively observed outside of the plasmasphere (Tsurutani & Smith, 1977), meanwhile plasmaspheric hiss and lightning generated whistlers are associated with the higher density region within the plasmasphere. To isolate chorus waves from various other wave modes, only observations outside of the plasmasphere are considered. To determine if a given observation was made inside or outside of the plamapause, the model initially proposed by Li, Thorne, Bortnik, et al. (2010) is used, whereby an observation is classified as outside if the total electron density falls below a threshold (N_c), where N_c is defined as:

$$N_c = \begin{cases} 50\ \text{cm}^{-3}, & \text{if } L > 4.4 \\ 10(6.6/L)^4\ \text{cm}^{-3} & \text{otherwise} \end{cases}$$

The THEMIS orbits extend beyond 10 R_E, where the satellites frequently cross the magnetopause and may remain outside of the magnetosphere for extended periods. In order to exclude emissions that originate from outside the magnetopause from our results, a model first proposed by Shue et al. (1998) is used and emissions observed while a given satellite is outside of the magnetopause are discarded.

3. Global Morphology of Chorus Waves Parametrized by f_{pe}/f_{ce}

The chorus wave intensity is binned into seven normalized frequency bands; from the lower hybrid frequency (f_{lhr}) to 0.1 f_{ce}, and from 0.1 f_{ce} to 0.7 f_{ce} in 0.1 f_{ce} increments. These are further binned into two $|\lambda_m|$ bins; <9° and 9–18°, three activity levels which we define as quiet (AE < 50 nT), moderate (50 < AE < 200 nT) and active (AE > 200 nT) and five local f_{pe}/f_{ce} bins; 2–4, 4–6, 6–8, 8–10, >10. The uncertainty in the f_{pe}/f_{ce} value will lead to some mixing of data points primarily between neighboring f_{pe}/f_{ce} bins. Finally, the data is binned into 0.1 L^* bins between 1 and 10, and hourly MLT bins. A wave database is then generated by combining data from all three THEMIS satellites, weighted by the number of samples in each bin. These bin ranges were chosen to ensure each variable demonstrated variability between bins, while also having a sufficient number of observations to provide good statistics in as many bins as possible.

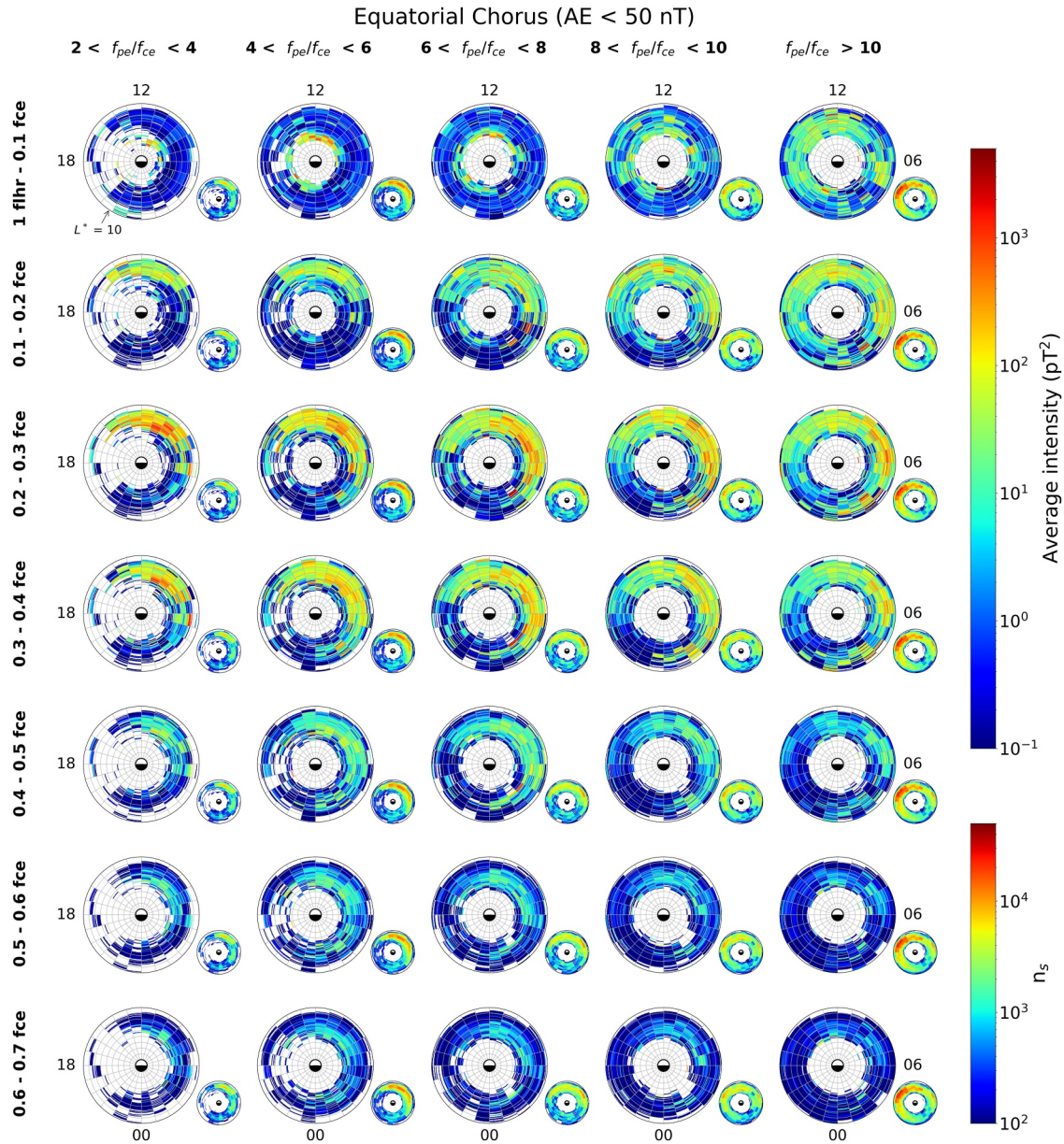

Figure 2. Global maps of the average chorus wave intensity during quiet geomagnetic conditions (AE < 50 nT) in the equatorial region ($|\lambda_m| < 9°$) as a function of L^* and magnetic local time for, from top to bottom, increasing relative frequency, and, from left to right, increasing f_{pe}/f_{ce}. The maps extend linearly out to $L^* = 10$ with noon at the top and dawn to the right. The average intensities are shown in the large panels and the corresponding sampling distributions in the small panels to the bottom right of each large panel.

3.1. Equatorial Chorus ($|\lambda_m| < 9°$)

The average chorus wave intensities in the equatorial region ($|\lambda_m| < 9°$) are plotted as a function of L^* and MLT for, from left to right, increasing f_{pe}/f_{ce} and, from top to bottom, increasing relative frequency, for quiet, moderate and active conditions in Figures 2–4 respectively. The main plots show the average chorus intensities and the smaller plots display the number of samples in each bin, defined here as the number of data points containing chorus waves observations. Each plot extends out to L^* of 10, with noon at the top and dawn to the right.

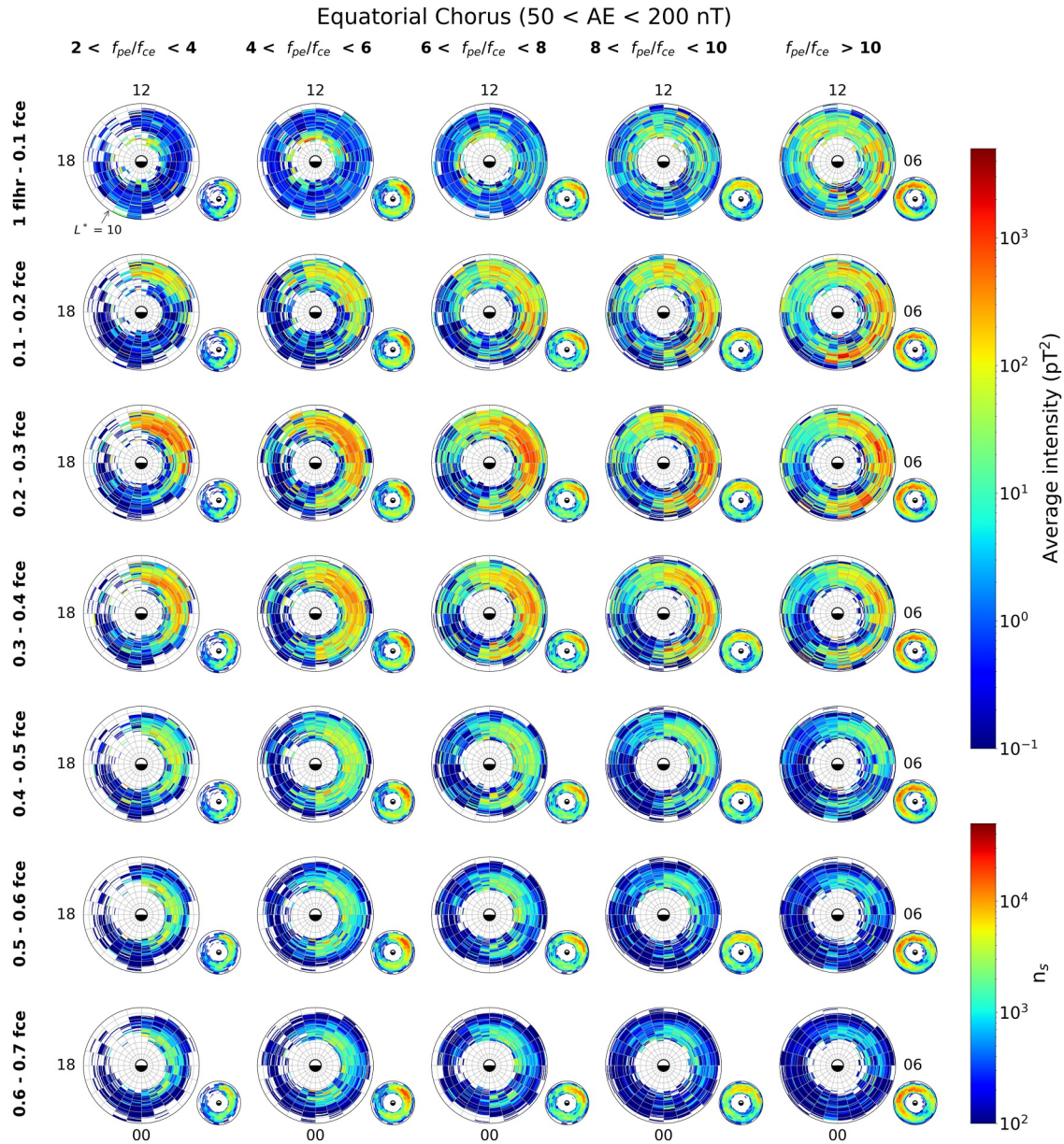

Figure 3. Global maps of the average chorus wave intensity during moderate geomagnetic conditions (50 nT < AE < 200 nT) in the equatorial region ($|\lambda_m| < 9°$) as a function of L^* and magnetic local time presented in the same format as Figure 2.

3.1.1. Low Frequency Chorus ($f_{lhr} < f < 0.1\,f_{ce}$)

Wave power is strongest in the lowest relative frequency band during active conditions and high values of f_{pe}/f_{ce} ($f_{pe}/f_{ce} > 10$) with average wave power typically greater than 100 pT^2 in the region of $5 < L^* < 8$ from 22:00 MLT through dawn to noon (see Figure 4). During quiet conditions weaker wave power is observed but the location is different with the waves seen predominantly from 21:00 through dusk to 09:00 MLT, again during high values of f_{pe}/f_{ce}.

3.1.2. Lower-Band Chorus

Lower-band chorus in the frequency range $0.1\,f_{ce} < f < 0.5\,f_{ce}$ peaks during active conditions, with the strongest emissions primarily spanning from 21:00 MLT through dawn to noon. At the low frequencies ($0.1\,f_{ce} < f < 0.2\,f_{ce}$), wave power also increases with increasing f_{pe}/f_{ce}, exceeding 300 pT^2 at large values of f_{pe}/f_{ce} ($f_{pe}/f_{ce} > 8$) in the

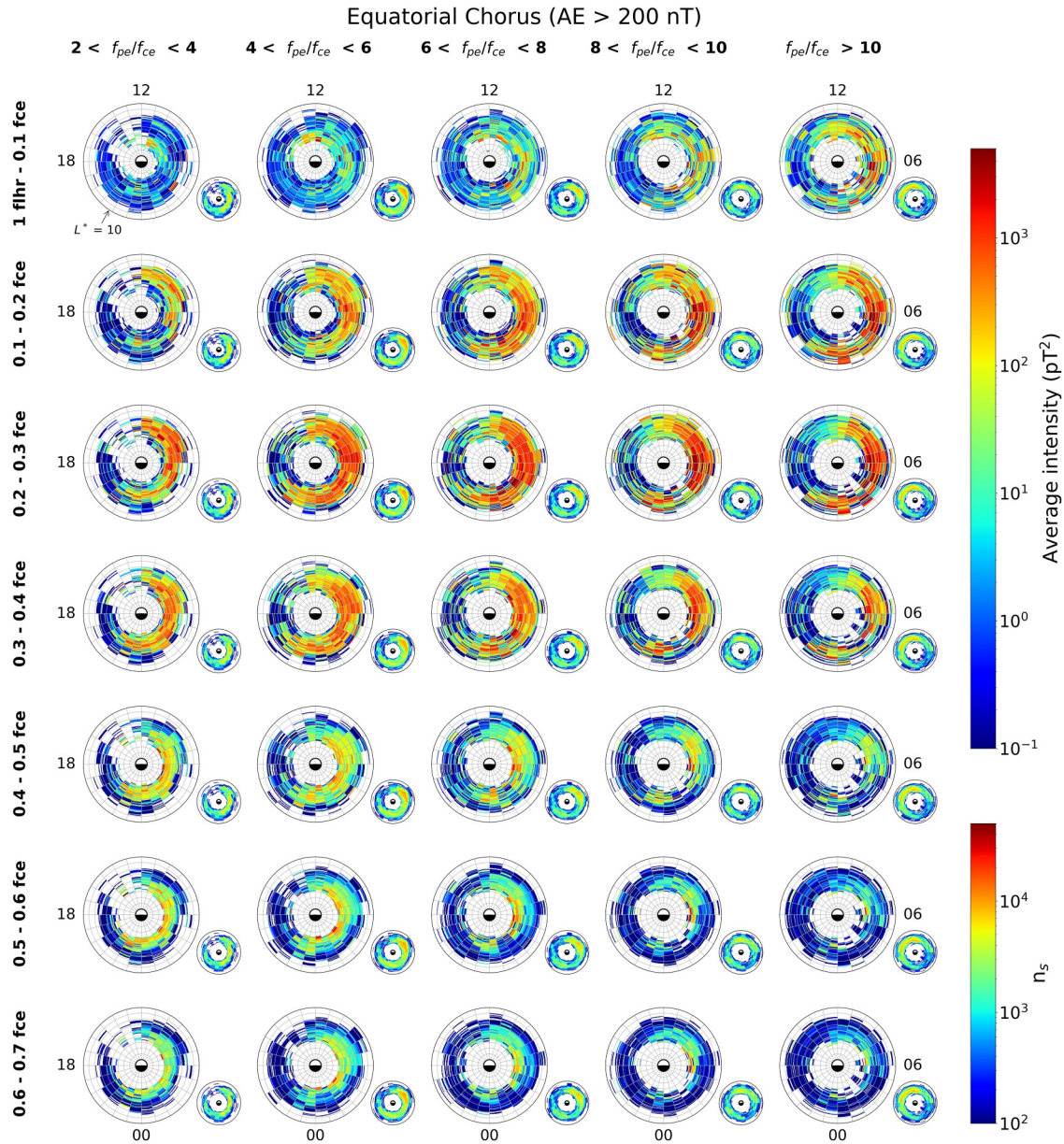

Figure 4. Global maps of the average wave chorus intensity during active geomagnetic conditions (AE > 200 nT) in the equatorial region ($|\lambda_m| < 9°$) as a function of L^* and magnetic local time presented in the same format as Figure 2.

region $5 < L^* < 8$. In sharp contrast, at high relative frequencies ($0.4\,f_{ce} < f < 0.5\,f_{ce}$), chorus intensities increase with decreasing f_{pe}/f_{ce}, exceeding 50 pT^2 when f_{pe}/f_{ce} is low ($f_{pe}/f_{ce} < 6$), predominantly in the region $4 < L^* < 6$ from 21:00–09:00 MLT. At intermediate frequencies ($0.3\,f_{ce} < f < 0.4\,f_{ce}$), wave power is largely independent of f_{pe}/f_{ce}, with intensities exceeding 100 pT^2, primarily in the region $3.5 < L^* < 8$ from 21:00 MLT through dawn to noon.

During quiet geomagnetic conditions the strongest emissions are observed in the frequency range $0.2\,f_{ce} < f < 0.3\,f_{ce}$ on the dayside in the region 08:00–15:00 MLT at low f_{pe}/f_{ce} ($f_{pe}/f_{ce} < 6$), with very little activity on the nightside at these times. In contrast, waves in this relative frequency range increase with increasing f_{pe}/f_{ce} in the region 00:00–08:00 MLT. At higher relative frequencies, $0.4\,f_{ce} < f < 0.5\,f_{ce}$ the emissions are weaker, with strongest emissions, of the order of 20 pT^2, being observed for $4 < f_{pe}/f_{ce} < 8$ from midnight through dawn to 15:00 MLT.

3.1.3. Upper-Band Chorus

Upper-band chorus generally intensifies with increasing activity and decreasing f_{pe}/f_{ce}, similar to lower-band chorus in the frequency range $0.4\ f_{ce} < f < 0.5\ f_{ce}$. The strongest upper-band emissions occur during active conditions at low f_{pe}/f_{ce} ($f_{pe}/f_{ce} < 6$), particularly in the $0.5\ f_{ce} < f < 0.6\ f_{ce}$ frequency band, where the wave intensities typically exceed 50 pT^2 in the region $4 < L^* < 6$ from 21:00 MLT through dawn to noon. With increasing f_{pe}/f_{ce}, the waves weaken and become more confined in MLT, being largely restricted to the post-dawn sector for $f_{pe}/f_{ce} > 8$.

During quiet geomagnetic conditions, upper-band chorus emissions are weak, with the strongest emissions, of the order 5–8 pT^2, being observed in the frequency range $0.5\ f_{ce} < f < 0.6\ f_{ce}$ predominantly at intermediate f_{pe}/f_{ce} values ($4 < f_{pe}/f_{ce} < 8$). As f_{pe}/f_{ce} increases, the strongest emissions become more constrained to the dayside and more specifically the post-dawn sector during both quiet and moderate geomagnetic conditions.

3.1.4. Multi-Variable Dependence of Chorus Wave Power

To better show the differences of chorus wave intensity with relative frequency, geomagnetic activity and f_{pe}/f_{ce}, Figure 5 shows the chorus wave intensity (B_w) averaged over all L^* regions weighted by number of samples in each bin, as a function of MLT for, from left to right, increasing geomagnetic activity and, top to bottom, increasing relative frequency. Each panel shows five traces, color-coded according to the value of f_{pe}/f_{ce}.

At low relative frequencies ($f_{lhr} < f < 0.2\ f_{ce}$), the strongest waves are seen during active geomagnetic conditions and high values of f_{pe}/f_{ce} ($f_{pe}/f_{ce} > 8$), where the wave power exceeds 100 pT^2 from midnight through dawn to noon. At intermediate relative frequencies ($0.3\ f_{ce} < f < 0.4\ f_{ce}$) the strongest waves are seen during active geomagnetic conditions, irrespective of the value of f_{pe}/f_{ce} with the wave power exceeding 100 pT^2 from approximately 22:00 MLT through dawn to midday. At high relative frequencies ($0.4\ f_{ce} < f < 0.6\ f_{ce}$) the strongest waves are seen during active conditions and low values of f_{pe}/f_{ce} ($f_{pe}/f_{ce} < 6$) where wave power exceeds 50 pT^2 from approximately 21:00 through dawn to 09:00 MLT.

During quiet geomagnetic activity the strongest lower band chorus emissions are largely confined to the dayside at low f_{pe}/f_{ce} ($f_{pe}/f_{ce} < 6$), with average intensities exceeding 100 pT^2 for $0.2\ f_{ce} < f < 0.3\ f_{ce}$ from 08:00–15:00 MLT. The power at higher values of f_{pe}/f_{ce} is typically lower by a factor of 2–5 in this region. On the nightside, the reverse is true with the strongest emissions, albeit less than 100 pT^2, at higher values of f_{pe}/f_{ce} being typically stronger than those at low f_{pe}/f_{ce} ($f_{pe}/f_{ce} < 4$) by a factor of 10 or more.

At higher frequencies the upper band chorus emissions are weak during quiet geomagnetic activity. At these times the strongest emissions are of the order 5–8 pT^2, in the frequency range $0.5\ f_{ce} < f < 0.6\ f_{ce}$, primarily for intermediate values of f_{pe}/f_{ce} ($4 < f_{pe}/f_{ce} < 8$) in the region from midnight through dawn to noon.

3.2. Off-Equatorial Chorus ($9 < |\lambda_m| < 18°$)

The average chorus intensities are shown as a function of relative frequency, location (L^*, MLT) and local f_{pe}/f_{ce} for quiet, moderate and active geomagnetic conditions in Figures 6–8 respectively. Figure 9, shows the average wave intensity across all L^* regions weighted by number of samples in each bin, against MLT for the off-equatorial ($9 < |\lambda_m| < 18°$) region.

Off-equatorial chorus is strongest in the lower band for relative frequencies in the range $0.1\ f_{ce} < f < 0.3\ f_{ce}$ and increases with increasing activity. The emissions are strongest during active conditions primarily in the region for $5 < L^* < 8$ from 06:00–15:00 MLT and are largely independent of f_{pe}/f_{ce} (see Figure 8). Similar trends are also seen for both quiet and moderate geomagnetic activity (see Figures 6 and 7). At higher relative frequencies the emissions in the off-equatorial region become weaker and are largely non-existent in the upper band. Low frequency chorus is also strongest during active conditions, primarily in the region 06:00–15:00 MLT for high f_{pe}/f_{ce} ($f_{pe}/f_{ce} > 6$). In contrast, during quiet conditions weak low frequency chorus emissions are observed from midday through dusk to 21:00 MLT, primarily for high values of f_{pe}/f_{ce} ($f_{pe}/f_{ce} > 10$).

Figure 9 illustrates that the MLT response of the lower and upper band chorus is relatively independent of f_{pe}/f_{ce}. This is particularly evident on the dayside, where the intensities tend to peak in the pre-noon sector. As the relative

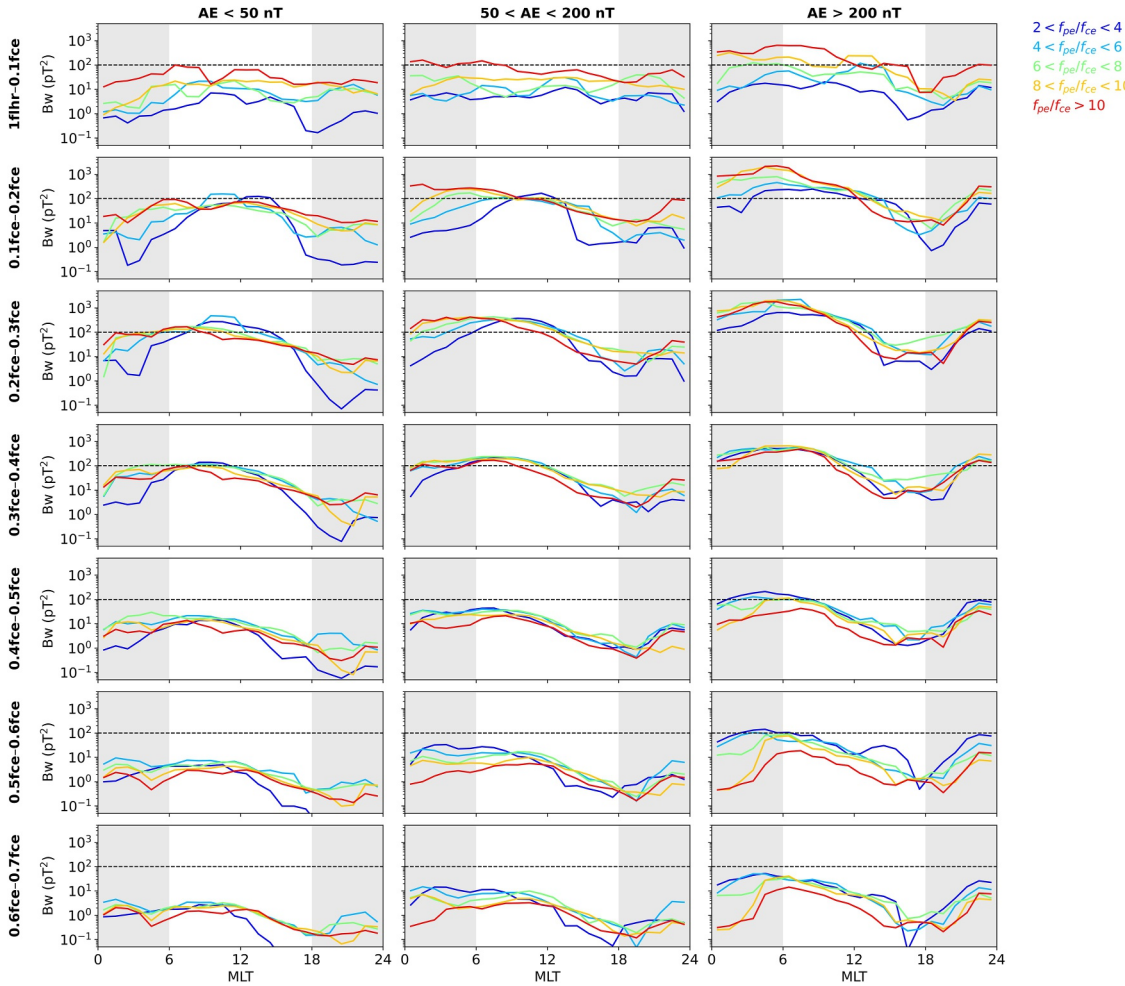

Figure 5. Equatorial ($|\lambda_m| < 9°$) chorus wave intensity as a function of magnetic local time, averaged over all L^* values for the selected f_{pe}/f_{ce} ranges (color-coded), for, from top to bottom, increasing relative frequency and, from left to right, increasing geomagnetic activity.

frequency increases, there is a general decline with the average wave intensity rarely exceeding 1 pT^2 at 0.6 $f_{ce} < f < 0.7\ f_{ce}$, regardless of geomagnetic activity or f_{pe}/f_{ce}. The most significant variations in wave intensities with f_{pe}/f_{ce} are visible on the nightside during periods of high geomagnetic activity. However, these variations are due to the poor statistical representation in this region, as seen in Figure 8. Notably, such disparities are not seen at lower activities.

There is mostly little to no chorus wave power on the nightside for all activity levels and values of f_{pe}/f_{ce}. The exceptions being during quiet and moderate conditions for high f_{pe}/f_{ce} ($f_{pe}/f_{ce} > 8$) when where weak power is observed in the frequency range $f_{lhr} < f < 0.2\ f_{ce}$ from 18:00–21:00 MLT and during moderate and active conditions for low f_{pe}/f_{ce} ($f_{pe}/f_{ce} < 6$) when stronger waves may be observed at low L^* in the frequency range 0.1 $f_{ce} < f < 0.3\ f_{ce}$ from 03:00–06:00 MLT.

4. Discussion

Chorus waves are generated outside of the plasmapause near the magnetic equator from 21:00 MLT through dawn to noon by anisotropic distributions of 1–100 keV electrons which are injected from the plasma sheet (Li, Thorne, Bortnik, et al., 2010; Omura et al., 2008). These electrons can cyclotron-resonate with chorus waves if they are above the minimum resonant energy ($E_{\min}$) (Horne & Thorne, 1998; Lyons & Thorne, 1972). Below this energy, electrons cannot efficiently interact with the wave. The strongest waves for a given normalized frequency are therefore likely to be observed when f_{pe}/f_{ce} is such that the $E_{\min}$ is in the range 1–100 keV.

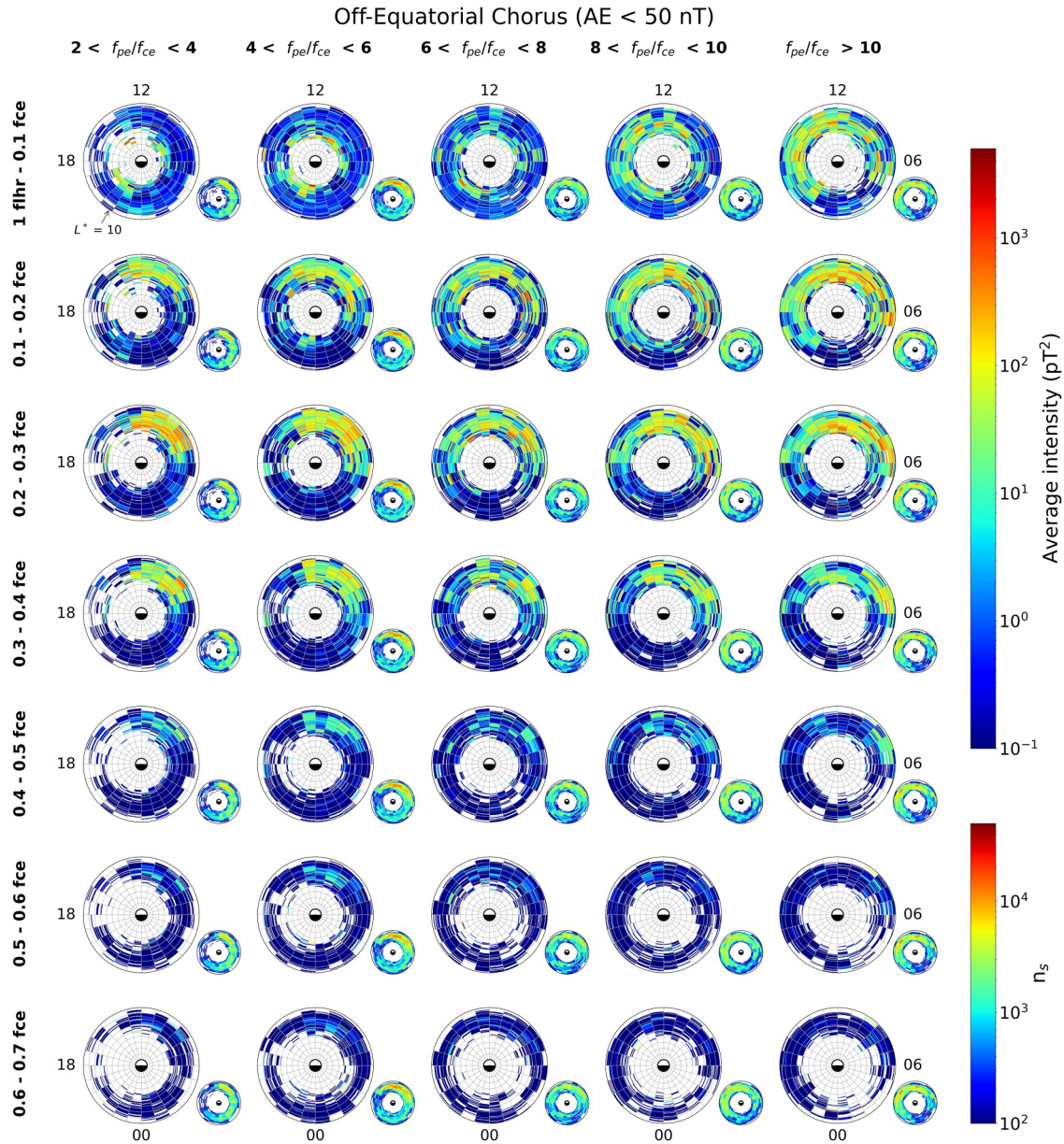

Figure 6. Global maps of the average chorus wave intensity during quiet geomagnetic conditions (AE < 50 nT) in the off-equatorial region ($9 < |\lambda_m| < 18°$) as a function of L^* and magnetic local time for, from top to bottom, increasing relative frequency, and, from left to right, increasing f_{pe}/f_{ce}. The maps extend linearly out to $L^* = 10$ with noon at the top and dawn to the right. The average intensities are shown in the large panels and the corresponding sampling distributions in the small panels to the bottom right of each large panel.

To determine the minimum resonant energy the method as outlined in Meredith et al. (2003) is applied. For electron interactions with parallel propagating chorus waves, only the fundamental cyclotron resonance occurs, and the relativistic resonance condition is as follows:

$$\omega - k_{\|} v_{\|} = \Omega_e / \gamma \tag{1}$$

where $\gamma = \left(1 - v^2/c^2\right)^{-1/2}$, $v^2 = v_{\perp}^2 + v_{\|}^2$ and c is the speed of light. Here $v_{\perp}$ and $v_{\|}$ are the electron velocities perpendicular and parallel to the ambient magnetic field, $\omega = 2\pi f$ is the wave frequency, $k_{\|}$ is the parallel wave number, and Ω_e is the electron gyrofrequency. For prescribed wave and plasma conditions, solutions for the resonant particle velocities lie along semi-ellipses in the $(v_{\perp}, v_{\|})$ plane. For a fixed wave frequency the minimum

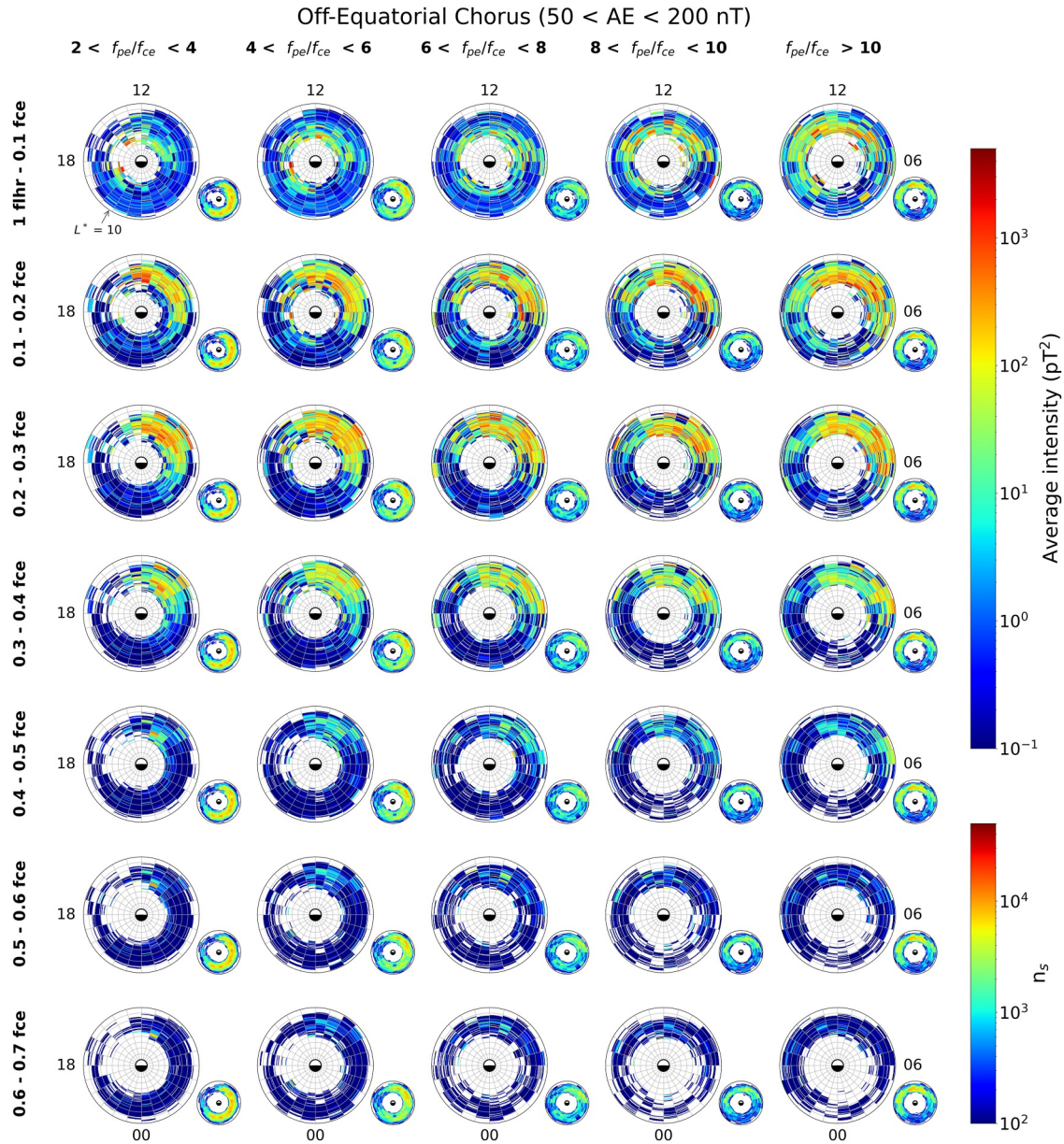

Figure 7. Global maps of the average chorus wave intensity during moderate geomagnetic conditions (50 nT < AE < 200 nT) in the off-equatorial region ($9 < |\lambda_m| < 18°$) as a function of L^* and magnetic local time presented in the same format as Figure 6.

resonant energy occurs when $v_\perp = 0$. The resonance condition can then be solved using the expression for $k_\parallel$ from the cold plasma dispersion relation for parallel propagating chorus waves in a proton-electron plasma, to yield an expression for the minimum parallel velocity as detailed in Meredith et al. (2003). The minimum parallel resonant energy is then determined by the resulting Lorentz factor ($E_{\min} = (\gamma - 1)m_e c^2$).

Plots of the minimum resonant energy as a function of f_{pe}/f_{ce} for selected relative frequencies (color-coded) are presented in Figure 10. Dashed horizontal lines are included to show 1 and 100 keV.

At low relative frequencies ($f_{lhr} < f < 0.1\, f_{ce}$) (top two traces in Figure 10) electrons with energies in the range 1–100 keV, can only efficiently interact with the waves at high values of f_{pe}/f_{ce}. This is consistent with the observations presented in Section 3, which shows the strongest waves in this frequency band are seen during active conditions for $5 < L^* < 8$ from 22:00–12:00 MLT at high values of f_{pe}/f_{ce} ($f_{pe}/f_{ce} > 10$).

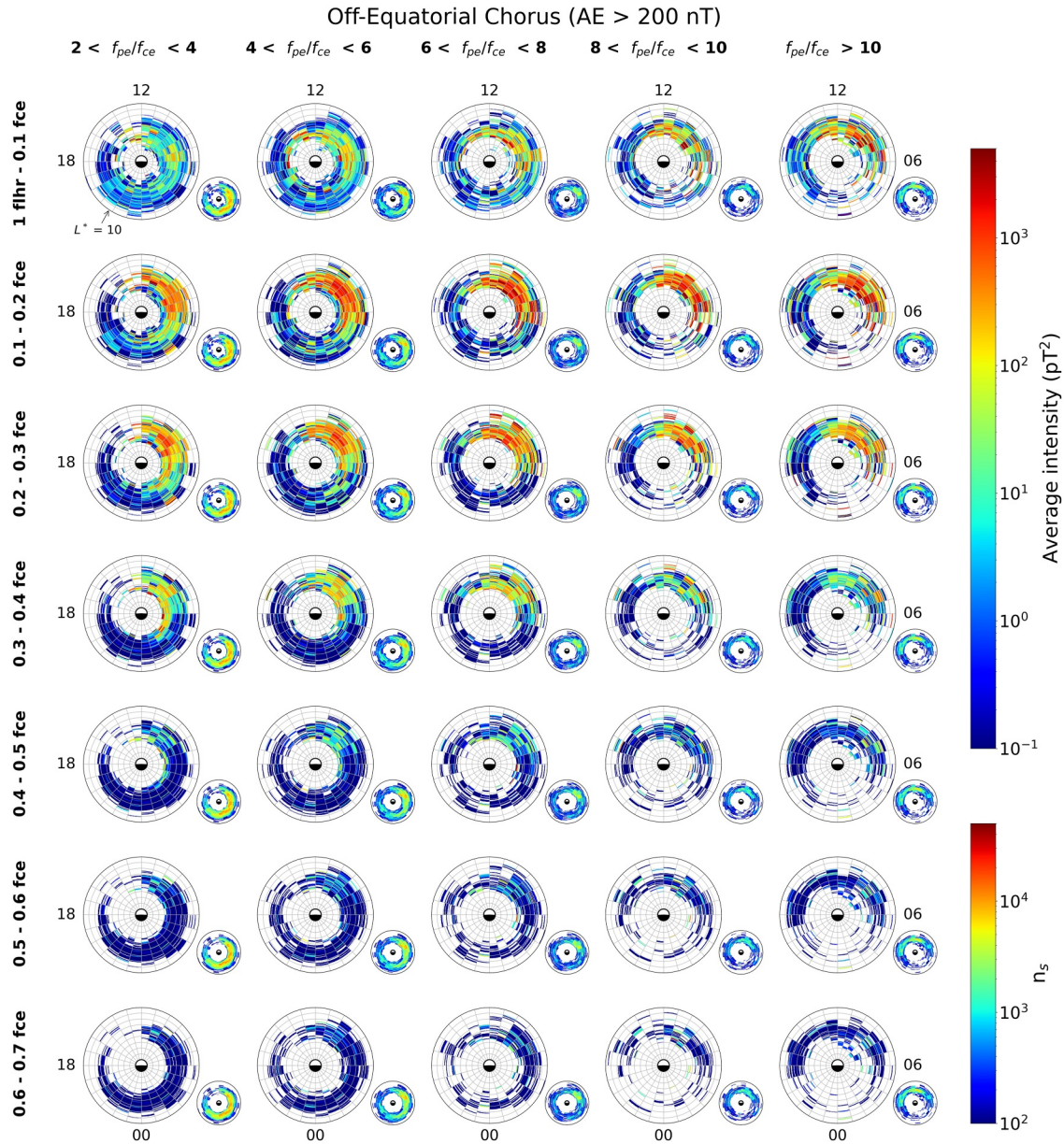

Figure 8. Global maps of the average chorus wave intensity during active geomagnetic conditions (AE > 200 nT) in the off-equatorial region ($9 < |\lambda_m| < 18°$) as a function of L^* and magnetic local time presented in the same format as Figure 6.

At intermediate relative frequencies ($0.3\,f_{ce} < f < 0.4\,f_{ce}$) (fourth and fifth traces from the top in Figure 10) electrons in the energy range 1–100 keV, can efficiently interact with the waves over a wide range of f_{pe}/f_{ce}. This is consistent with the observations presented in Section 3, which demonstrate the strongest waves are independent of f_{pe}/f_{ce}, with similar intensities and MLT distribution across the range of f_{pe}/f_{ce} values used in this study.

At high relative frequencies ($0.5\,f_{ce} < f < 0.7\,f_{ce}$) (bottom three traces in Figure 10), electrons with energies in the 1–100 keV range can efficiently interact with the waves at low values of f_{pe}/f_{ce}. This is once again consistent with the observations presented in Section 3, which demonstrates the strongest waves are seen during active conditions for $4 < L^* < 6$ from 21:00–09:00 MLT at low values of f_{pe}/f_{ce} ($f_{pe}/f_{ce} < 6$).

During low and moderate activity, weak emissions (~10 pT^2) are found at low relative frequencies ($f_{lhr} < f < 0.1\,f_{ce}$) on the dayside extending from approximately 12:00–20:00 MLT at high f_{pe}/f_{ce} ($f_{pe}/f_{ce} > 8$). These emissions are unlikely to be chorus emissions since they are observed in a completely different region to the low frequency

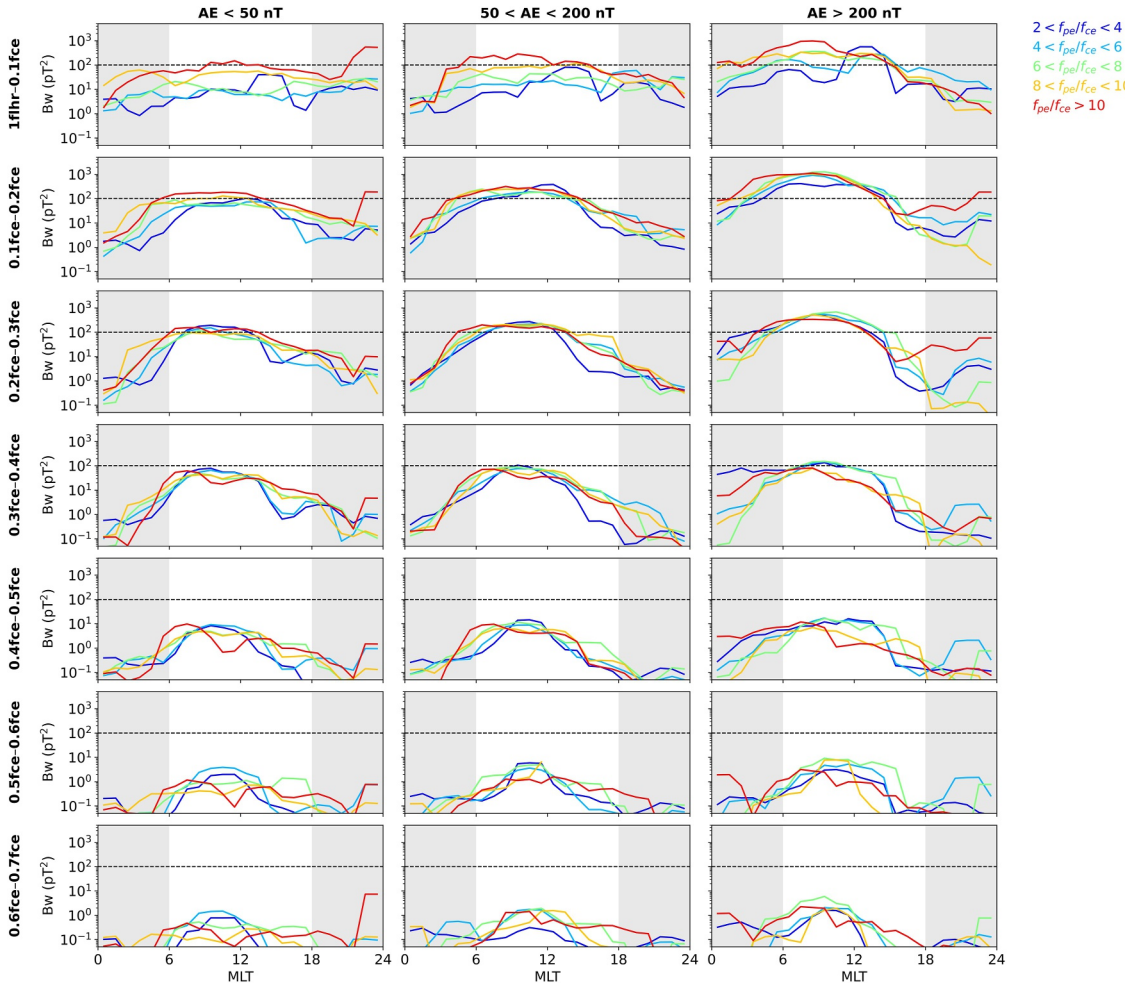

Figure 9. Off-Equatorial ($9 < |\lambda_m| < 18°$) chorus wave intensity as a function of magnetic local time, averaged over all L^* values for the selected f_{pe}/f_{ce} ranges (color-coded), for, from top to bottom, increasing relative frequency and, from left to right, increasing geomagnetic activity.

chorus which is observed during active conditions and the lower-band and upper-band chorus during quiet, moderate and active conditions. These emissions occur in a similar frequency range and cover a similar MLT range as exohiss (e.g., Russell et al., 1969; Seo & Kim, 2023; Thorne et al., 1973; J. L. Wang et al., 2020; Watt et al., 2025; Zhu et al., 2015, 2019), which is itself formed by the leakage of plasmaspheric hiss from the plasmasphere and out into the plasmatrough. Our results suggest an activity dependence of the low frequency waves ($f_{lhr} < f < 0.1\, f_{ce}$), ranging from predominantly exohiss during quiet conditions to chorus during active conditions. This is further supported by the fact that the MLT distribution during moderate conditions shows features consistent with both exohiss and chorus. Our observations show that exohiss is strongest at high values of f_{pe}/f_{ce}, suggesting that the waves, when present, enhance pitch angle scattering. This supports previous findings that exohiss contributes to electron loss processes only (e.g., Li et al., 2019; Zou et al., 2024).

The energization of electrons to relativistic energies is most efficient in regions where large lower-band chorus wave intensities, of the order of several hundred pT^2 are observed in regions of low f_{pe}/f_{ce} (typically $f_{pe}/f_{ce} < 4$), (e.g., Horne et al., 2005; Horne & Thorne, 2003; Meredith et al., 2003). In the equatorial region ($|\lambda_m| < 9°$) the most favorable conditions for acceleration occur during active periods for waves in the intermediate relative frequency range ($0.2\, f_{ce} < f < 0.4\, f_{ce}$), from midnight through to noon. Strong waves in regions of low f_{pe}/f_{ce} are also observed at higher latitudes ($9 < |\lambda_m| < 18°$) where the most favorable conditions occur for waves in the frequency range $0.1\, f_{ce} < f < 0.3\, f_{ce}$ for $5 < L^* < 8$ between 06:00–15:00 MLT.

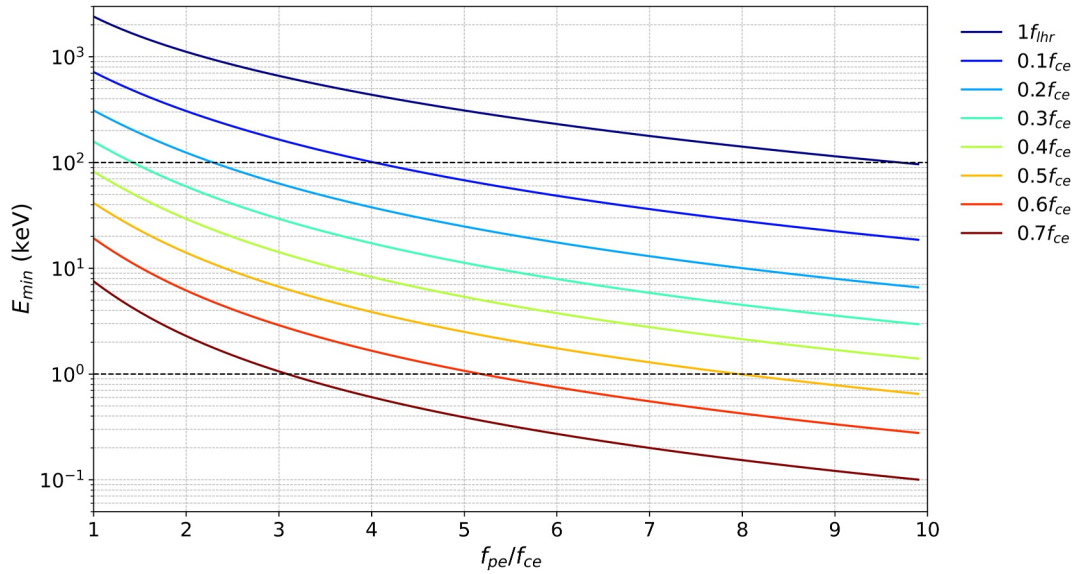

Figure 10. Plots of minimum resonant energy, $E_{\min}$, as a function of f_{pe}/f_{ce} for selected relative frequencies (color coded).

Regions of high f_{pe}/f_{ce} ($f_{pe}/f_{ce} > 8$) do not result in efficient transfer of energy to seed electrons and are largely responsible for pitch angle scattering. Therefore, it would be expected that the strong low frequency waves observed between f_{lhr} and $0.4\,f_{ce}$ during active conditions in the most post-midnight sector in regions of high f_{pe}/f_{ce} would be largely responsible for electron loss.

We stress that knowledge of the location and wave intensity alone are not sufficient to determine favorable regions for electron acceleration to relativistic energies. The knowledge of the local value of f_{pe}/f_{ce} is also required. The f_{pe}/f_{ce} ratio can span a wide range of values even for a particular location and activity level. This emphasizes the importance of using co-located measurements of both wave and plasma properties when deriving diffusion coefficients. At intermediate relative frequencies ($0.3\,f_{ce} < f < 0.4\,f_{ce}$), results show that the spatial distribution of chorus waves is independent of f_{pe}/f_{ce}, further demonstrating that geomagnetic activity alone does not determine the plasma environment.

To help understand the role of chorus in electron acceleration, we must also take into account the temporal behavior of f_{pe}/f_{ce} during a geomagnetic storm at different locations in space. Typically, during the main phase of the storm, the plasmatrough becomes depleted and then subsequently refills during the recovery phase. Previous observations by the Van Allen Probes have shown to that densities near $L = 6$ can increase from 2 cm^{-3} at the Dst minimum to over 25 cm^{-3} within one day (Bishop & Blum, 2024). This corresponds to an f_{pe}/f_{ce} increase starting at <4, and extending to >10. This rapid plasmatrough refilling rate is consistent with estimates by a machine learning model trained on THEMIS observations (Chu et al., 2017). This large variability in the f_{pe}/f_{ce} ratio implies that during a geomagnetic storm, chorus may drive efficient acceleration during the early recovery phase of the storm when f_{pe}/f_{ce} is low (<4), before tending toward a scattering-dominated regime when density and f_{pe}/f_{ce} become large (>10) and acceleration effectively stops. This behavior is consistent with observations of rapid relativistic electron flux enhancements soon after storm minimum, followed by slower increases later in recovery (e.g., Pinto et al., 2018; Varotsou et al., 2008). We note that this current study does not capture temporal evolution however, these results highlight the importance of incorporating plasmatrough refilling and thus plasmapause dynamics into future models.

Near-equatorial chorus in the $0.1\,f_{ce} < f < 0.3\,f_{ce}$ frequency range becomes increasingly confined to the dayside as f_{pe}/f_{ce} decreases during periods of low to moderate geomagnetic activity. In contrast, during active conditions, strong emissions in this frequency range at low f_{pe}/f_{ce} are also observed on the nightside, consistent with substorm injections. The absence of comparable nightside activity during low and moderate geomagnetic activity reflects the lack of substorm injections, while the restriction of strong chorus wave intensity to the dayside is likely reflective of drift-dependent effects.

In the mid-latitude region, strong chorus is primarily restricted to the dayside during active conditions at relative frequencies in the range $0.1\,f_{ce} < f < 0.3\,f_{ce}$. There is very little chorus activity on the night side at any relative frequency with the notable exception of low relative frequencies and low L^* from midnight to dawn. This is consistent with previous studies (e.g., Koons & Roeder, 1990; Meredith et al., 2012, 2020; Tsurutani & Smith, 1977). Nightside damping rates are much stronger than that on the dayside due to higher fluxes of suprathermal electrons, which mostly prevents the chorus waves from reaching higher latitudes in this region (Bortnik et al., 2007). Damping rates decrease with decreasing frequency and decreasing L^* which can explain the observations of the waves primarily observed at lower relative frequencies on the dayside and also at the lower relative frequencies on the nightside closer to the planet (Bortnik et al., 2007).

5. Conclusions

In this study, approximately 24.5 years of combined THEMIS wave data were analyzed to investigate how the spatial location and intensity of chorus waves vary with relative frequency, geomagnetic activity and local f_{pe}/f_{ce}, enabling the identification of regions which are most favorable for electron acceleration up to MeV energies. The main findings of this study are:

1. At low relative frequencies ($f_{lhr} < f < 0.1\,f_{ce}$) the strongest waves in the equatorial region are seen during active conditions in the region $5 < L^* < 8$, from 22:00 MLT through dawn to noon at high values of f_{pe}/f_{ce} ($f_{pe}/f_{ce} > 10$).
2. At intermediate relative frequencies ($0.3\,f_{ce} < f < 0.4\,f_{ce}$), the strongest waves in the equatorial region are seen during active conditions in the region $3.5 < L^* < 8$, from 21:00 MLT through dawn to noon and are largely independent of f_{pe}/f_{ce}.
3. At high relative frequencies ($0.5\,f_{ce} < f < 0.7\,f_{ce}$), the strongest waves in the equatorial region are seen during active conditions in the region $4 < L^* < 6$, from 21:00 MLT through dawn to 09:00 MLT at low values of f_{pe}/f_{ce} ($f_{pe}/f_{ce} < 6$).
4. In the off-equatorial region the strongest waves are seen in the frequency range $0.1\,f_{ce} < f < 0.3\,f_{ce}$ between $5 < L^* < 8$, and 06:00–15:00 MLT and are largely independent of f_{pe}/f_{ce}.
5. The frequencies of the strongest waves in the equatorial source region are consistent with the resonant frequencies of injected electrons in the energy range 1–100 keV.
6. The location of the strongest waves can be largely explained in terms of the source electrons being in the required energy range for resonance and the absence of Landau damping.
7. Electron acceleration to relativistic energies will be most effective when strong lower band chorus is observed in regions of low f_{pe}/f_{ce}. In the equatorial region these conditions can be met primarily for waves in the frequency range $0.2\,f_{ce} < f < 0.4\,f_{ce}$ from 21:00 MLT through dawn to noon. At higher latitudes these conditions can be met on the dayside from 06:00–15:00 MLT for waves in the frequency range $0.1\,f_{ce} < f < 0.3\,f_{ce}$.

Overall, this study highlights the critical role of f_{pe}/f_{ce} on the spatial distribution and dynamic behavior of chorus waves under varying geomagnetic conditions, as well as its influence on wave-particle interactions. During a geomagnetic storm f_{pe}/f_{ce} outside of the plasmapause may gradually change from low to high values over the course of the recovery phase (Bishop & Blum, 2024; Chu et al., 2017), suggesting that the role of chorus may change from efficient acceleration early in the recovery phase to little or no acceleration and even loss toward the end of the recovery phase.

Conflict of Interest

The authors declare no conflicts of interest relevant to this study.

Data Availability Statement

The THEMIS data used in this study is publicly available from http://themis.ssl.berkeley.edu/data/themis/ and the AE index is publicly available from https://omniweb.gsfc.nasa.gov/. The results and data shown in this study can be downloaded from the UK Polar Data Centre at Bunting et al. (2026).

Acknowledgments
We thank NASA Contract NAS5-02099 and V. Angelopoulos for use of data from THEMIS mission. Specifically, we thank O. Le Contel and the late A. Roux for use of SCM data, J. W. Bonnell and F. S. Mozer for use of EFI data, C. W. Carlson and J. P. McFadden for use of ESA data and K. H. Glassmeier, U. Auster and W. Baumjohann for the use of FGM data provided under the lead of the Technical University of Braunschweig and with financial support through the German Ministry for Economy and Technology and the German Center for Aviation and Space (DLR) under contract 50 OC 0302. We acknowledge the NSSDC Omniweb for the provision of the geomagnetic activity indices used in this report. The research leading to these results has received funding from the Natural Environment Research Council Grants NE/X000389/1 and NE/R016038/1. JB and RM gratefully acknowledge NASA/LWs award 80NSSC22K1023 through the University of Colorado, Boulder, and 80NSSC22K1637 from the University of Texas at Dallas. QM was supported by the NASA Grants 80NSSC24K0572 and 80NSSC26K0123, and the NSF Grant AGS-2225445. XS would like to acknowledge the NASA Grants 80NSSC24K0266 and 80NSSC24K0239, and NSF Grants AGS-2225445 and AGS-2247774.

References

Abel, B., & Thorne, R. M. (1998a). Electron scattering loss in Earth's inner magnetosphere: 1. Dominant physical processes. *Journal of Geophysical Research*, *103*(A2), 2385–2396. https://doi.org/10.1029/97JA02919

Abel, B., & Thorne, R. M. (1998b). Electron scattering loss in Earth's inner magnetosphere: 2. Sensitivity to model parameters. *Journal of Geophysical Research*, *103*(A2), 2397–2407. https://doi.org/10.1029/97JA02920

Agapitov, O., Mourenas, D., Artemyev, A., Hospodarsky, G., & Bonnell, J. (2019). Time scales for electron quasi-linear diffusion by lower-band chorus waves: The effects of ω_{pe}/Ω_{ce} dependence on geomagnetic activity. *Geophysical Research Letters*, *46*(12), 6178–6187. https://doi.org/10.1029/2019GL083446

Agapitov, O. V., Mourenas, D., Artemyev, A. V., Mozer, F. S., Hospodarsky, G., Bonnell, J., & Krasnoselskikh, V. (2018). Synthetic empirical chorus wave model from combined Van Allen probes and cluster statistics. *Journal of Geophysical Research: Space Physics*, *123*(1), 297–314. https://doi.org/10.1002/2017JA024843

Albert, J. M. (1994). Quasi-linear pitch angle diffusion coefficients: Retaining high harmonics. *Journal of Geophysical Research*, *99*(A12), 23741–23745. https://doi.org/10.1029/94JA02345

Allison, H. J., Shprits, Y. Y., Zhelavskaya, I. S., Wang, D., & Smirnov, A. G. (2021). Gyroresonant wave-particle interactions with chorus waves during extreme depletions of plasma density in the Van Allen radiation belts. *Science Advances*, *7*(5), eabc0380. https://doi.org/10.1126/sciadv.abc0380

Angelopoulos, V. (2008). The THEMIS Mission. *Space Science Reviews*, *141*(1–4), 5–34. https://doi.org/10.1007/s11214-008-9336-1

Auster, H. U., Glassmeier, K. H., Magnes, W., Aydogar, O., Baumjohann, W., Constantinescu, D., et al. (2008). The THEMIS fluxgate magnetometer. *Space Science Reviews*, *141*(1–4), 235–264. https://doi.org/10.1007/s11214-008-9365-9

Bishop, T. B., & Blum, L. W. (2024). Global maps of plasmaspheric erosion and refilling for varying geomagnetic conditions. *Journal of Geophysical Research: Space Physics*, *129*(9), e2024JA032587. https://doi.org/10.1029/2024JA032587

Bortnik, J., Li, W., Thorne, R. M., Angelopoulos, V., Cully, C., Bonnell, J., et al. (2009). An observation linking the origin of plasmaspheric hiss to discrete chorus emissions. *Science*, *324*(5928), 775–778. https://doi.org/10.1126/science.1171273

Bortnik, J., Thorne, R. M., & Meredith, N. P. (2007). Modeling the propagation characteristics of chorus using CRRES suprathermal electron fluxes. *Journal of Geophysical Research*, *112*(A8), A08204. https://doi.org/10.1029/2006JA012237

Bortnik, J., Thorne, R. M., & Meredith, N. P. (2008). The unexpected origin of plasmaspheric hiss from discrete chorus emissions. *Nature*, *452*(7183), 62–66. https://doi.org/10.1038/nature06741

Bunting, K., Meredith, N., Bortnik, J., Ma, Q., Matsuura, R., & Shen, X. (2026). Global morphology of chorus waves in the outer radiation belt and the effect of geomagnetic activity and fpe/fce (version 1.0) [Dataset]. *NERC EDS UK Polar Data Centre*. https://doi.org/10.5285/5586a319-fa57-4bb6-af3a-3746cd643c0d

Burtis, W. J., & Helliwell, R. A. (1969). Banded chorus—a new type of VLF radiation observed in the magnetosphere by OGO 1 and OGO 3. *Journal of Geophysical Research (1896-1977)*, *74*(11), 3002–3010. https://doi.org/10.1029/JA074i011p03002

Chu, X. N., Bortnik, J., Li, W., Ma, Q., Angelopoulos, V., & Thorne, R. M. (2017). Erosion and refilling of the plasmasphere during a geomagnetic storm modeled by a neural network. *Journal of Geophysical Research: Space Physics*, *122*(7), 7118–7129. https://doi.org/10.1002/2017JA023948

Cully, C. M., Ergun, R. E., Stevens, K., Nammari, A., & Westfall, J. (2008). The THEMIS digital fields board. *Space Science Reviews*, *141*(1–4), 343–355. https://doi.org/10.1007/s11214-008-9417-1

Feng, B., Li, H., Yu, X., Yuan, Z., Tang, R., Wang, D., et al. (2023). The evolution of whistler hiss-like waves across plasmapause: Hiss to exohiss. *Geophysical Research Letters*, *50*(8), e2023GL102993. https://doi.org/10.1029/2023GL102993

Glauert, S. A., & Horne, R. B. (2005). Calculation of pitch angle and energy diffusion coefficients with the PADIE code. *Journal of Geophysical Research*, *110*(A4), A04206. https://doi.org/10.1029/2004JA010851

Glauert, S. A., Horne, R. B., & Meredith, N. P. (2014). Three-dimensional electron radiation belt simulations using the BAS radiation belt model with new diffusion models for chorus, plasmaspheric hiss, and lightning-generated whistlers. *Journal of Geophysical Research: Space Physics*, *119*(1), 268–289. https://doi.org/10.1002/2013JA019281

Graham, R. (1994). Killer electrons on rise. *Albuquerque Journal B*, *8*, 15.

Horne, R. B., Glauert, S. A., & Thorne, R. M. (2003). Resonant diffusion of radiation belt electrons by whistler-mode chorus. *Geophysical Research Letters*, *30*(9), 1493. https://doi.org/10.1029/2003GL016963

Horne, R. B., Kersten, T., Glauert, S. A., Meredith, N. P., Boscher, D., Sicard-Piet, A., et al. (2013). A new diffusion matrix for whistler mode chorus waves. *Journal of Geophysical Research: Space Physics*, *118*(10), 6302–6318. https://doi.org/10.1002/jgra.50594

Horne, R. B., & Thorne, R. M. (1998). Potential waves for relativistic electron scattering and stochastic acceleration during magnetic storms. *Geophysical Research Letters*, *25*(15), 3011–3014. https://doi.org/10.1029/98GL01002

Horne, R. B., & Thorne, R. M. (2003). Relativistic electron acceleration and precipitation during resonant interactions with whistler-mode chorus. *Geophysical Research Letters*, *30*(10), 1527. https://doi.org/10.1029/2003GL016973

Horne, R. B., Thorne, R. M., Shprits, Y. Y., Meredith, N. P., Glauert, S. A., Smith, A. J., et al. (2005). Wave acceleration of electrons in the Van Allen radiation belts. *Nature*, *437*(7056), 227–230. https://doi.org/10.1038/nature03939

Inan, U. S., Platino, M., Bell, T. F., Gurnett, D. A., & Pickett, J. S. (2004). Cluster measurements of rapidly moving sources of ELF/VLF chorus. *Journal of Geophysical Research*, *109*(A5), A05214. https://doi.org/10.1029/2003JA010289

Jaynes, A. N., Baker, D. N., Singer, H. J., Rodriguez, J. V., Loto'aniu, T. M., Ali, A. F., et al. (2015). Source and seed populations for relativistic electrons: Their roles in radiation belt changes. *Journal of Geophysical Research: Space Physics*, *120*(9), 7240–7254. https://doi.org/10.1002/2015JA021234

Koons, H., & Roeder, J. (1990). A survey of equatorial magnetospheric wave activity between 5 and 8 R_E. *Planetary and Space Science*, *38*(10), 1335–1341. https://doi.org/10.1016/0032-0633(90)90136-e

Kwon, H.-J., Kim, K.-H., Jee, G., Park, J.-S., Jin, H., & Nishimura, Y. (2015). Plasmapause location under quiet geomagnetic conditions ($Kp \leq 1$): THEMIS observations. *Geophysical Research Letters*, *42*(18), 7303–7310. https://doi.org/10.1002/2015GL066090

Lam, M. M., Horne, R. B., Meredith, N. P., & Glauert, S. A. (2007). Modeling the effects of radial diffusion and plasmaspheric hiss on outer radiation belt electrons. *Geophysical Research Letters*, *34*(20), L20112. https://doi.org/10.1029/2007GL031598

Lauben, D. S., Inan, U. S., Bell, T. F., & Gurnett, D. A. (2002). Source characteristics of ELF/VLF chorus. *Journal of Geophysical Research*, *107*(A12), SMP10-1–17. https://doi.org/10.1029/2000JA003019

Le Contel, O., Roux, A., Robert, P., Coillot, C., Bouabdellah, A., de La Porte, B., et al. (2008). First results of the THEMIS search coil magnetometers. *Space Science Reviews*, *141*(1–4), 509–534. https://doi.org/10.1007/s11214-008-9371-y

Li, W., Shen, X.-C., Ma, Q., Capannolo, L., Shi, R., Redmon, R. J., et al. (2019). Quantification of energetic electron precipitation driven by plume whistler mode waves, plasmaspheric hiss, and exohiss. *Geophysical Research Letters*, *46*(7), 3615–3624. https://doi.org/10.1029/2019GL082095

Li, W., Thorne, R. M., Angelopoulos, V., Bortnik, J., Cully, C. M., Ni, B., et al. (2009). Global distribution of whistler-mode chorus waves observed on the THEMIS spacecraft. *Geophysical Research Letters*, *36*(9), L09104. https://doi.org/10.1029/2009GL037595

Li, W., Thorne, R. M., Bortnik, J., Nishimura, Y., Angelopoulos, V., Chen, L., et al. (2010). Global distributions of suprathermal electrons observed on THEMIS and potential mechanisms for access into the plasmasphere. *Journal of Geophysical Research*, *115*(A12), A00J10. https://doi.org/10.1029/2010JA015687

Li, W., Thorne, R. M., Bortnik, J., Tao, X., & Angelopoulos, V. (2012). Characteristics of hiss-like and discrete whistler-mode emissions. *Geophysical Research Letters*, *39*(18), L18106. https://doi.org/10.1029/2012GL053206

Li, W., Thorne, R. M., Nishimura, Y., Bortnik, J., Angelopoulos, V., McFadden, J. P., et al. (2010). THEMISanalysis of observed equatorial electron distributions responsible for the chorus excitation. *Journal of Geophysical Research*, *115*(A6), A00F11. https://doi.org/10.1029/2009JA014845

Lorentzen, K. R., Blake, J. B., Inan, U. S., & Bortnik, J. (2001). Observations of relativistic electron microbursts in association with VLF chorus. *Journal of Geophysical Research*, *106*(A4), 6017–6027. https://doi.org/10.1029/2000JA003018

Lyons, L. R., & Thorne, R. M. (1972). Parasitic pitch angle diffusion of radiation belt particles by ion cyclotron waves. *Journal of Geophysical Research (1896-1977)*, *77*(28), 5608–5616. https://doi.org/10.1029/JA077i028p05608

Lyons, L. R., & Thorne, R. M. (1973). Equilibrium structure of radiation belt electrons. *Journal of Geophysical Research (1896-1977)*, *78*(13), 2142–2149. https://doi.org/10.1029/JA078i013p02142

Lyons, L. R., Thorne, R. M., & Kennel, C. F. (1972). Pitch-angle diffusion of radiation belt electrons within the plasmasphere. *Journal of Geophysical Research (1896-1977)*, *77*(19), 3455–3474. https://doi.org/10.1029/JA077i019p03455

Ma, Q., Li, W., Thorne, R. M., Bortnik, J., Reeves, G. D., Kletzing, C. A., et al. (2016). Characteristic energy range of electron scattering due to plasmaspheric hiss. *Journal of Geophysical Research: Space Physics*, *121*(12), 11737–11749. https://doi.org/10.1002/2016JA023311

Ma, Q., Xu, W., Sanchez, E. R., Marshall, R. A., Bortnik, J., Reyes, P. M., et al. (2022). Analysis of electron precipitation and ionospheric density enhancements due to hiss using incoherent scatter radar and Arase observations. *Journal of Geophysical Research: Space Physics*, *127*(8), e2022JA030545. https://doi.org/10.1029/2022JA030545

Malaspina, D. M., Jaynes, A. N., Hospodarsky, G., Bortnik, J., Ergun, R. E., & Wygant, J. (2017). Statistical properties of low-frequency plasmaspheric hiss. *Journal of Geophysical Research: Space Physics*, *122*(8), 8340–8352. https://doi.org/10.1002/2017JA024328

Meredith, N. P., Horne, R. B., & Anderson, R. R. (2001). Substorm dependence of chorus amplitudes: Implications for the acceleration of electrons to relativistic energies. *Journal of Geophysical Research*, *106*(A7), 13165–13178. https://doi.org/10.1029/2000JA900156

Meredith, N. P., Horne, R. B., Bortnik, J., Thorne, R. M., Chen, L., Li, W., & Sicard-Piet, A. (2013). Global statistical evidence for chorus as the embryonic source of plasmaspheric hiss. *Geophysical Research Letters*, *40*(12), 2891–2896. https://doi.org/10.1002/grl.50593

Meredith, N. P., Horne, R. B., Glauert, S. A., & Anderson, R. R. (2007). Slot region electron loss timescales due to plasmaspheric hiss and lightning-generated whistlers. *Journal of Geophysical Research*, *112*(A8), A08214. https://doi.org/10.1029/2007JA012413

Meredith, N. P., Horne, R. B., Glauert, S. A., Baker, D. N., Kanekal, S. G., & Albert, J. M. (2009). Relativistic electron loss timescales in the slot region. *Journal of Geophysical Research*, *114*(A3), A03222. https://doi.org/10.1029/2008JA013889

Meredith, N. P., Horne, R. B., Glauert, S. A., Thorne, R. M., Summers, D., Albert, J. M., & Anderson, R. R. (2006). Energetic outer zone electron loss timescales during low geomagnetic activity. *Journal of Geophysical Research*, *111*(A5), A05212. https://doi.org/10.1029/2005JA011516

Meredith, N. P., Horne, R. B., Shen, X.-C., Li, W., & Bortnik, J. (2020). Global model of whistler mode chorus in the near-equatorial region ($|\lambda m| < 18°$). *Geophysical Research Letters*, *47*(11), e2020GL087311. https://doi.org/10.1029/2020GL087311

Meredith, N. P., Horne, R. B., Sicard-Piet, A., Boscher, D., Yearby, K. H., Li, W., & Thorne, R. M. (2012). Global model of lower band and upper band chorus from multiple satellite observations. *Journal of Geophysical Research*, *117*(A10), A10225. https://doi.org/10.1029/2012JA017978

Meredith, N. P., Horne, R. B., Summers, D., Thorne, R. M., Iles, R. H. A., Heynderickx, D., & Anderson, R. R. (2002). Evidence for acceleration of outer zone electrons to relativistic energies by whistler mode chorus. *Annales Geophysicae*, *20*(7), 967–979. https://doi.org/10.5194/angeo-20-967-2002

Meredith, N. P., Thorne, R. M., Horne, R. B., Summers, D., Fraser, B. J., & Anderson, R. R. (2003). Statistical analysis of relativistic electron energies for cyclotron resonance with EMIC waves observed on CRRES. *Journal of Geophysical Research*, *108*(A6), 1250. https://doi.org/10.1029/2002JA009700

Min, K., Lee, J., Keika, K., & Li, W. (2012). Global distribution of EMIC waves derived from THEMIS observations. *Journal of Geophysical Research*, *117*(A5), A05219. https://doi.org/10.1029/2012JA017515

Miyoshi, Y., Kataoka, R., Kasahara, Y., Kumamoto, A., Nagai, T., & Thomsen, M. F. (2013). High-speed solar wind with southward interplanetary magnetic field causes relativistic electron flux enhancement of the outer radiation belt via enhanced condition of whistler waves. *Geophysical Research Letters*, *40*(17), 4520–4525. https://doi.org/10.1002/grl.50916

Mozer, F. S. (1973). Analysis of techniques for measuring DC and AC electric fields in the magnetosphere. *Space Science Reviews*, *14*(2), 272–313. https://doi.org/10.1007/BF02432099

Namekawa, T., Mitani, T., Asamura, K., Miyoshi, Y., Hosokawa, K., Lessard, M., et al. (2023). Simultaneous precipitation of sub-relativistic electron microburst and pulsating aurora electrons. *Geophysical Research Letters*, *50*(24), e2023GL104001. https://doi.org/10.1029/2023GL104001

Nishimura, Y., Bortnik, J., Li, W., Thorne, R. M., Lyons, L. R., Angelopoulos, V., et al. (2010). Identifying the driver of pulsating aurora. *Science*, *330*(6000), 81–84. https://doi.org/10.1126/science.1193186

Omura, Y., Katoh, Y., & Summers, D. (2008). Theory and simulation of the generation of whistler-mode chorus. *Journal of Geophysical Research*, *113*(A4), A04223. https://doi.org/10.1029/2007JA012622

Pedersen, A., Mozer, F., & Gustafsson, G. (1998). Electric field measurements in a tenuous plasma with spherical double probes. In *Measurement techniques in space plasmas* (pp. 1–12). American Geophysical Union (AGU). https://doi.org/10.1002/9781118664391.ch1

Pinto, V. A., Kim, H.-J., Lyons, L. R., & Bortnik, J. (2018). Interplanetary parameters leading to relativistic electron enhancement and persistent depletion events at geosynchronous orbit and potential for prediction. *Journal of Geophysical Research: Space Physics*, *123*(2), 1134–1145. https://doi.org/10.1002/2017JA024902

Roux, A., Le Contel, O., Coillot, C., Bouabdellah, A., de La Porte, B., Alison, D., et al. (2008). The search coil magnetometer for THEMIS. *Space Science Reviews*, *141*(1–4), 265–275. https://doi.org/10.1007/s11214-008-9455-8

Russell, C. T., Holzer, R. E., & Smith, E. J. (1969). OGO 3 observations of ELF noise in the magnetosphere: 1. spatial extent and frequency of occurrence. *Journal of Geophysical Research (1896-1977)*, *74*(3), 755–777. https://doi.org/10.1029/JA074i003p00755

Santolík, O., Gurnett, D. A., Pickett, J. S., Parrot, M., & Cornilleau-Wehrlin, N. (2003). Spatio-temporal structure of storm-time chorus. *Journal of Geophysical Research*, *108*(A7), 1278. https://doi.org/10.1029/2002JA009791

Santolík, O., Němec, F., Gereová, K., Macúšová, E., de Conchy, Y., & Cornilleau-Wehrlin, N. (2004). Systematic analysis of equatorial noise below the lower hybrid frequency. *Annales Geophysicae*, *22*(7), 2587–2595. https://doi.org/10.5194/angeo-22-2587-2004

Seo, J., & Kim, K.-C. (2023). The relationship of exohiss waves with plasmaspheric hiss distribution and solar wind parameters. *Journal of Geophysical Research: Space Physics*, *128*(10), e2023JA031777. https://doi.org/10.1029/2023JA031777

Shue, J.-H., Song, P., Russell, C. T., Steinberg, J. T., Chao, J. K., Zastenker, G., et al. (1998). Magnetopause location under extreme solar wind conditions. *Journal of Geophysical Research*, *103*(A8), 17691–17700. https://doi.org/10.1029/98JA01103

Summers, D., Mace, R. L., & Hellberg, M. A. (2005). Pitch-angle scattering rates in planetary magnetospheres. *Journal of Plasma Physics*, *71*(3), 237–250. https://doi.org/10.1017/S0022377804003186

Summers, D., Ni, B., & Meredith, N. P. (2007a). Timescales for radiation belt electron acceleration and loss due to resonant wave-particle interactions: 1. Theory. *Journal of Geophysical Research*, *112*(A4), A04206. https://doi.org/10.1029/2006JA011801

Summers, D., Ni, B., & Meredith, N. P. (2007b). Timescales for radiation belt electron acceleration and loss due to resonant wave-particle interactions: 2. Evaluation for VLF chorus, ELF hiss, and electromagnetic ion cyclotron waves. *Journal of Geophysical Research*, *112*(A4), A04207. https://doi.org/10.1029/2006JA011993

Summers, D., Thorne, R. M., & Xiao, F. (1998). Relativistic theory of wave-particle resonant diffusion with application to electron acceleration in the magnetosphere. *Journal of Geophysical Research*, *103*(A9), 20487–20500. https://doi.org/10.1029/98JA01740

Thorne, R. M. (2010). Radiation belt dynamics: The importance of wave-particle interactions. *Geophysical Research Letters*, *37*(22), L22107. https://doi.org/10.1029/2010GL044990

Thorne, R. M., Li, W., Ni, B., Ma, Q., Bortnik, J., Chen, L., et al. (2013). Rapid local acceleration of relativistic radiation-belt electrons by magnetospheric chorus. *Nature*, *504*(7480), 411–414. https://doi.org/10.1038/nature12889

Thorne, R. M., O'Brien, T. P., Shprits, Y. Y., Summers, D., & Horne, R. B. (2005). Timescale for MeV electron microburst loss during geomagnetic storms. *Journal of Geophysical Research*, *110*(A9), A09202. https://doi.org/10.1029/2004JA010882

Thorne, R. M., Smith, E. J., Burton, R. K., & Holzer, R. E. (1973). Plasmaspheric hiss. *Journal of Geophysical Research (1896-1977)*, *78*(10), 1581–1596. https://doi.org/10.1029/JA078i010p01581

Tsurutani, B. T., & Smith, E. J. (1977). Two types of magnetospheric ELF chorus and their substorm dependences. *Journal of Geophysical Research (1896-1977)*, *82*(32), 5112–5128. https://doi.org/10.1029/JA082i032p05112

Tsyganenko, N. A., & Sitnov, M. I. (2005). Modeling the dynamics of the inner magnetosphere during strong geomagnetic storms. *Journal of Geophysical Research*, *110*(A3), A03208. https://doi.org/10.1029/2004JA010798

Varotsou, A., Friedel, R. H., Reeves, G. D., Lavraud, B., Skoug, R. M., Cayton, T. E., & Bourdarie, S. (2008). Characterization of relativistic electron flux rise times during the recovery phase of geomagnetic storms as measured by the NS41 GPS satellite. *Journal of Atmospheric and Solar-Terrestrial Physics*, *70*(14), 1745–1759. https://doi.org/10.1016/j.jastp.2008.01.020

Wang, J. L., Li, L. Y., & Yu, J. (2020). Statistical relationship between exohiss waves and plasmaspheric hiss. *Geophysical Research Letters*, *47*(5), e2020GL087023. https://doi.org/10.1029/2020GL087023

Wang, J.-Z., Hu, Y.-Q., Yu, D.-Y., Cai, Z.-B., & Zhang, Q.-X. (2018). Electron environment characteristics and internal charging evaluation for MEO satellite. *IEEE Transactions on Nuclear Science*, *65*(8), 1685–1693. https://doi.org/10.1109/TNS.2018.2792049

Watt, C. E. J., Meredith, N. P., Wong, J., Murphy, K. R., Rae, I. J., Chakraborty, S., et al. (2025). Occurrence rates and variability of whistler-mode waves in the plasma trough. *Journal of Geophysical Research: Space Physics*, *130*(10), e2025JA034061. https://doi.org/10.1029/2025JA034061

Wong, J.-M., Meredith, N. P., Horne, R. B., Glauert, S. A., & Ross, J. P. J. (2024). New chorus diffusion coefficients for radiation belt modeling. *Journal of Geophysical Research: Space Physics*, *129*(1), e2023JA031607. https://doi.org/10.1029/2023JA031607

Wrenn, G. L., Rodgers, D. J., & Ryden, K. A. (2002). A solar cycle of spacecraft anomalies due to internal charging. *Annales Geophysicae*, *20*(7), 953–956. https://doi.org/10.5194/angeo-20-953-2002

Zhu, H., Gu, W., & Chen, L. (2019). Statistical analysis on plasmatrough exohiss waves from the van allen probes. *Journal of Geophysical Research: Space Physics*, *124*(6), 4356–4364. https://doi.org/10.1029/2018JA026359

Zhu, H., Su, Z., Xiao, F., Zheng, H., Wang, Y., Shen, C., et al. (2015). Plasmatrough exohiss waves observed by Van Allen probes: Evidence for leakage from plasmasphere and resonant scattering of radiation belt electrons. *Geophysical Research Letters*, *42*(4), 1012–1019. https://doi.org/10.1002/2014GL062964

Zou, W., Li, H., Hu, P., Wang, D., Tang, R., Ouyang, Z., et al. (2024). Statistical properties of exohiss waves and associated scattering losses of radiation belt electrons. *Journal of Geophysical Research: Space Physics*, *129*(5), e2023JA032244. https://doi.org/10.1029/2023JA032244